crystals

MDPI

Article

Advancing Bulk Growth of 100 mm AlN by Physical Vapor Transport

Robert T. Bondokov [1,*], Shogen Matsumoto [1,2], Connor G. Carr [1], Kasey Hogan [1], Griffin Q. Norbury [1], Masato Kobayashi [3] and James Grandusky [1]

[1] Crystal IS, Inc., Green Island, NY 12183, USA
[2] Next Generation Compound Semiconductor Development Department, Asahi Kasei Corporation, Fuji 416-8501, Japan
[3] Production Technology Center, Asahi Kasei Corporation, Kawasaki 210-0863, Japan
* Correspondence: bondokov@cisuvc.com

Abstract

Ultrawide bandgap (UWBG) semiconductors are destined to become the foundation for next-generation power and radio-frequency (RF) electronic devices. Their superior qualities such as high thermal conductivity, strong critical electric field, and robust mechanical and radiation hardness are driving continuous and widespread research. Amongst the UWBG materials, aluminum nitride (AlN) is highly attractive due to its direct ultrawide bandgap of about 6.2 eV, resulting in one of the highest Baliga's and Johnson's figures of merit. Equally important as its properties are material availability and growth methods capable of producing large-diameter substrates. In this work we report on bulk growth of 100 mm AlN crystals using the physical vapor transport (PVT) technique. The thermal gradients were simulated and tailored to obtain adequate thermal stresses, resulting in substrates with narrow X-ray rocking curves and dislocation densities in the range of 10^2–10^5 cm^{-2}. In addition, the room-temperature thermal conductivity measured in two directions, perpendicular and parallel to the *c*-axis, was confirmed to be 300 W m^{-1} K^{-1}. AlN substrates also demonstrated high UV transparency with absorption coefficients as low as 10 cm^{-1} at 265 nm wavelength. These results, along with the availability of 100 mm substrates, demonstrate that AlN is ready for further exploration and development for the power and RF electronics industry.

Keywords: AlN; crystal growth; dislocation; thermal conductivity; semiconductor; shear stress; etching; physical vapor transport; slip system; simulation

Check for updates

Academic Editor: Evgeniy N. Mokhov

Received: 6 August 2026
Revised: 26 August 2026
Accepted: 31 August 2026
Published: 2 September 2026

Copyright: © 2026 by the authors. Licensee MDPI, Basel, Switzerland. This article is an open access article distributed under the terms and conditions of the Creative Commons Attribution (CC BY) license.

1. Introduction

The rapid advancement of aluminum nitride (AlN) materials and device research is indicative of the growing maturity and commercial potential of AlN-based technology. This maturation reflects both the exceptional AlN properties, such as ultrawide bandgap, high thermal conductivity, high critical electric field, and high chemical and mechanical endurance, as well as the progress in AlN substrate industrialization that has enabled research and device manufacturing. Historically, the limited availability of AlN substrates was one of the key barriers to the adoption of AlN as a viable ultrawide bandgap (UWBG) material [1]. In 2021, 2-inch AlN substrates became available in large quantities [2]. Meanwhile, the continuous advancements in crystal growth led to the development of the first 100 mm AlN substrates [3].

Numerous research groups have reported electronic device structures utilizing AlN substrates, with the majority being high-electron-mobility transistors (HEMTs) but research was also conducted on metal-semiconductor field-effect transistors (MESFETs) and Schottky diodes. Very recently, HEMT structures grown on AlN single-crystal substrates demonstrated radio-frequency (RF) device characteristics comparable to the state-of-the-art gallium nitride (GaN) HEMT [4]. Such structures show a lower dislocation density by a factor of about 10^6 in the epi-layer as well as a higher thermal boundary conductance at the growth interface when compared to the conventional HEMT. Additionally, the utilization of an *n*-type δ-doping layer between the AlN buffer and GaN channel in the AlN/GaN/AlN heterostructures was shown to improve the conductivity of the two-dimensional electron gas (2DEG) and achieve a structure with low sheet resistance [5]. In another study [6], the importance of the AlN substrate was further emphasized in accomplishing a state-of-the-art 2DEG mobility of 1805 $cm^2\ V^{-1}\ s^{-1}$ for a 150 nm thick channel. Lee reported low sheet resistance, high-breakdown field, and current-collapse-free AlN/GaN/AlN HEMTs grown by metalorganic vapor-phase epitaxy (MOVPE) on AlN substrates [7]. Aluminum nitride substrates enabled achievement of high-breakdown voltage in the forming of Schottky barriers [8,9], as well as in AlN-on-AlN MESFETs [10]. The very recent results reported by Jamil et al. [11] emphasized the key role of the AlN substrate in achieving a record forward current density of 14 kA cm^{-2} and high breakdown field of 8.3 MV cm^{-1} in quasi-vertical Schottky diodes.

Availability of AlN substrates with at least 100 mm diameter is a critical prerequisite for the continued development and commercial deployment of AlN and related structures for electronic devices. Consequently, significant research efforts have been devoted, in recent years, to the advancement of AlN bulk crystal growth technology. For instance, Hartmann et al. successfully developed a technique to expand the AlN crystal diameter while preserving the crystal quality [12], which is a key for further progress of this material growth system. Similar efforts led to obtaining crystals with diameters larger than 2 inch [13,14] and even reaching 3 inch [15,16]. A recent study [17] described the achievement of a 4-inch AlN ingot. However, this material exhibited very wide X-ray diffraction (XRD) rocking curves with a full width at half maximum (FWHM) range of 277 to 446 arcsec, making it essentially a non-single crystal. Likewise, the authors in ref. [18] used the PVT technique to obtain a 4-inch crystal, with limited structural quality. Another approach to increase substrate diameter is to form an AlN template on 4- and 6-inch sapphire wafers [19,20]. However, the dislocation densities for such structures remain above 10^8 cm^{-2}. In this report, we communicate the recent advances of the bulk growth of state-of-the-art AlN single crystals with 100 mm diameter.

2. Theoretical and Experimental Background

Aluminum nitride crystals were grown by the physical vapor transport (PVT) technique. The fundamentals of the technique were previously described [21] while the specifics on crystal diameter expansion to 100 mm were also detailed [3]. The PVT process is the most investigated and productive method to grow AlN single crystals. This process requires placing a native seed in a crucible that is heated above 2000 °C. The AlN seed can be oriented so that either Al- or N-polar faces are exposed to the incoming vapor. Our current setup uses Al-polar seeds that are placed on the colder side of a tungsten crucible. A thermal gradient is built by means of thermal insulation, shielding, and positioning of the crucible with respect to the heater. Key factors in growing larger crystals include nucleation, hot-zone design, mass transfer, crystal diameter expansion, and thermal field construction. While all of these aspects are important, the thermal field plays the central role in crystal growth. Increasing the seed surface area (e.g., from ~2 inch to ~100 mm) and, at the same

time, keeping the growth rate constant requires a higher sublimation rate. This can be accomplished using a compound approach of power increase and hot-zone improvements aiming for better vertical heat extraction. These components account for an increase in thermal gradients in both axial and radial directions. In general, if no specific actions are taken, the increase in thermal gradients is associated with an increase in their curvature, in which case the thermal stress increase within the crystal is inevitable. The crystal diameter increase itself is expected to result in an even bigger thermal stress increase [3]. Increased thermal gradients and their curvature can be correlated with increased dislocation density, crystal fracture, and lattice bending.

The thermal stress within the crystal can have different origins and can be generated during different growth stages. A few instances include coefficient of thermal expansion (CTE) mismatch between the growing crystal and growth cell materials, presence of flaws (inclusions, voids, etc.) within the crystal matrix, as well as nonuniform heat flow dissipation during crystallization and/or cool-down stages. Since AlN crystallizes in a wurtzite structure with hexagonal rotational symmetry and is grown along the c-axis, an axisymmetric model having stress tensor main components as σ_{rr}, σ_{zz}, $\sigma_{\varphi\varphi}$, and σ_{rz} can be used for analysis (Figure 1a). Furthermore, shear stress is used to evaluate the internal forces responsible for dislocation glide, twist, material tear, and other failure modes. With respect to single crystals, the component of the applied stress (compressive or tensile) resolved onto a specific slip system is routinely used as it represents the actual portion of an external load exerted on a specific crystallographic slip system (Figure 1b).

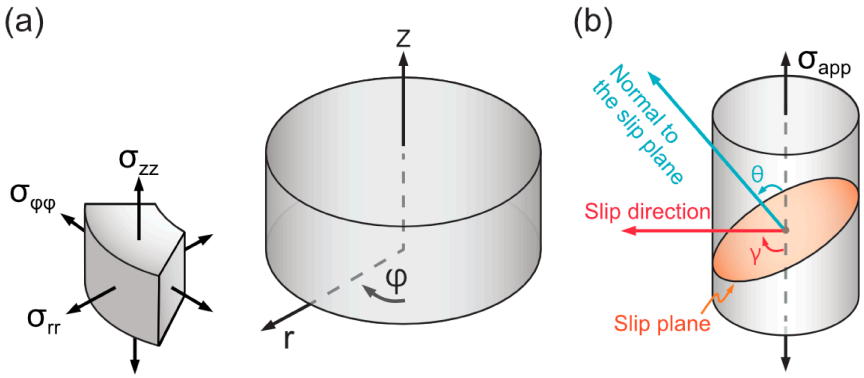

Figure 1. Schematic representation of (**a**) the stress tensor components and (**b**) resolved shear stress.

Therefore, the resolved shear stress (RSS), τ_{RS}, is expressed as:

$$\tau_{RS} = S \times \sigma_{app} = \sigma_{app} \cos\gamma \cos\theta, \quad (1)$$

where S is the Schmid factor, σ_{app} is the applied tensile stress, θ is the angle between the normal to the slip plane and the stress direction, and γ is angle between the slip direction and applied stress direction. According to Schmid's law (also called critical shear stress law), when the resolved shear stress reaches an acute value called critical resolved shear stress (CRSS), the onset of plastic deformation occurs [22]. According to this law, the critical resolved shear stress for all slip systems is the same, so the slip system with the highest Schmid factor would yield first. Such a slip system is called a primary slip system; however, it should be noted that if the stress is increased beyond the yield stress (the stress causing slip on the primary slip system), other slip systems may get activated.

Besides the highest Schmid factor, the primary slip system for a single crystal may be determined by an estimation based on specific lattice parameters, but experimental determination is always preferable. For aluminum nitride crystallizing in the wurtzite structure, the ratio between the lattice constants *c* and *a* is about 1.6. Since $\frac{c}{a} < 1.63$, the

prismatic glide system $\langle 11\bar{2}0\rangle\{1\bar{1}00\}$ would likely be the primary one [23]. This assumption was confirmed by Zhao et al. whose molecular dynamics simulation determined the easiest glide system to be the prismatic one, followed by the basal and pyramidal glide systems [24]. Experimentally, preferable prismatic slip was observed for AlN ceramics in the temperature range 500–800 °C [25]. For AlN single crystals, prismatic slip bands were the first evidence of the prismatic glide system being favorably activated [23,26]. Not long ago, prismatic glide in AlN single crystals was reported by Hu et al. [27,28]. In their comprehensive study on the role of the residual stress in defect formation, Herms et al. also corroborated the activation of the prismatic slip [29].

2.1. Critical Resolved Shear Stress Estimation

The most reliable way to obtain critical resolved shear stress is to measure the engineering stress–strain curves for different temperatures, strain rates, and sample orientations. As an emerging semiconductor, the AlN lacks such empirical data as opposed to, for example, more mature silicon carbide (SiC) [30]. Instead, one could estimate the Peierls (Peierls–Nabarro) stress [27,28] as it defines the minimum shear stress needed to establish dislocation movement within a plane of atoms (i.e., glide). The Peierls stress for dislocations at 0 K (τ_0) is estimated by using the following expression [31]:

$$\tau_0 = \frac{E_0}{(1+\nu)(1-\nu)} e^{-\frac{2\pi d}{(1-\nu)b}} \quad (2)$$

Here, d and b indicate the plane spacing and the magnitude of the Burgers vector. E_0 and ν are Young's modulus and Poisson's ratio in AlN, respectively. The temperature dependency of Peierls stress (τ_T) can be described using melting point (T_m):

$$\frac{\tau_T}{\tau_0} = \frac{E_T}{E_0}\frac{T_m}{13\,T} e^{-\frac{2\pi d}{(1-\nu)b}} \quad (3)$$

By using Equations (2) and (3), we can obtain the Peierls stresses for the edge dislocations with Burgers vector magnitude $\frac{1}{3}a$. Numerical simulations of the heat and mass transfer were utilized to calculate the thermal field within the growth cell. T_m of AlN is reported in the range of 2500–2700 °C [21,32]. Other parameters of AlN for these calculations were used from our previous report [21].

Furthermore, the critical resolved shear stress can be estimated using the homology model for tetra-bonded crystals proposed by Kirchner and Suzuki [33]. They observed that, for the semiconductor crystals with corner-sharing tetrahedra and sp^3 hybridization, the temperature dependence of the CRSS, $\tau_{CRS}(T)$, obeys the following universal relationship: all $\tau_{CRS}(T)$ datapoints lie on one and the same master curve. This curve can be expressed as:

$$\frac{\tau_{CRS}}{G} = f\left(\frac{kT}{Gb^3}\right), \quad (4)$$

where k is the Boltzmann constant and G is the shear modulus of the material. Using the plot generated by the Kirchner and Suzuki homology model we can estimate the CRSS in AlN single crystals as a function of temperature (Figure 2). As expected, the critical resolved shear stress follows an exponential decay with a typical fitting error ±1 MPa [34]. Both types of estimates, the Peierls stress and homology model, return values of τ_{RSS} well below 20 MPa, which suggests the possibility of crystallographic glide at growth temperature. Table 1 summarizes the data for the critical resolved shear stress estimation for a temperature range that covers the relevant growth temperatures, T_G, for AlN grown using PVT, as well as the temperatures slightly below the T_G which are likely sufficient to activate the conservative dislocation movement. The wide data range additionally

emphasizes the need for experimental τ_{RSS} measurements that are expected to become available in the near future.

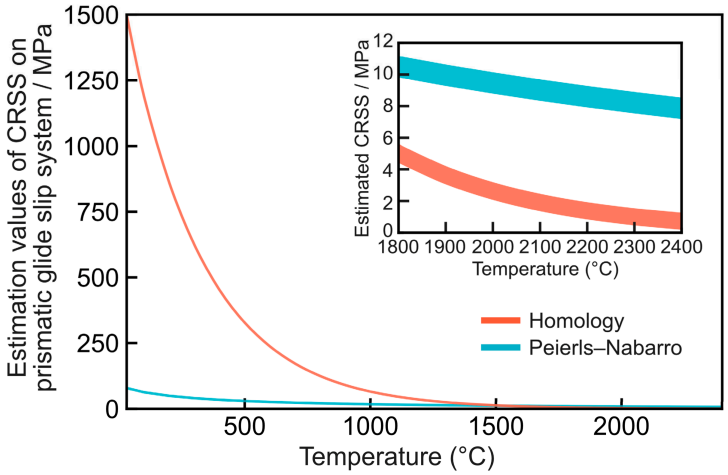

Figure 2. The stresses used for yield point comparison: Peierls stresses for the TED AlN crystal and CRSS estimation using homology model.

Table 1. Estimated values of the CRSS of AlN single crystals for the relevant temperature range 1800–2400 °C.

	τ_{PN}/MPa	τ_{PN}/MPa	$\tau_{Homology}$/MPa	τ_{MD}/MPa
CRSS	7.8–11.2	6.6–9.0	0.2–5.8	583–1430
Source	This work	[28]	This work	[24]

The τ_{PN} represents the Peierls–Nabarro stress estimated using the experimental law of temperature dependency; $\tau_{Homology}$ represents the CRSS calculated using homology model; τ_{MD} stands for the extrapolated values of the CRSS temperature dependence.

2.2. Numerical Simulations of the Resolved Shear Stress for Prismatic and Basal Slip Systems

Based on the fundamental and classical theory of thermal elasticity of materials with rigid bodies [35,36], governing equations for resolved shear stress can be described as:

$$\nabla\left\{\overline{\overline{C}} : \left(\overline{\overline{e}}(U)\right) - \overline{\overline{\beta}}(T - T_{Ref})\right\} = 0 \quad (5)$$

Here, $\overline{\overline{C}}$ and $\overline{\overline{\beta}}$ are the stress–strain tensor and thermal expansion tensor of AlN, respectively. $\overline{\overline{e}}(U)$ is the total strain tensor. T and T_{Ref} are the temperature for each mesh points and reference temperature, which is obtained as average temperature in the crystal. The ΔT is defined as T subtracted by T_{Ref}. PVT-based crystal growth is a combination of multi-physics phenomena, which makes simulation challenging. Therefore, for simplicity, one can simulate the global temperature field within the crystal at the growth stage by two-dimensional axisymmetric finite-element-method (2D-FEM) simulation tools. Such tools originated for PVT growth of SiC and have been extensively used for simulation of AlN crystal growth; some examples include the following studies [37–42]. Our simulations were carried out using the whole setup including the crucible, the hot-zone insulation, as well as the chamber. Figure 3 shows the contour plot of ΔT distributions in the crystal at the growth stage in the 2-inch and 100 mm crystal growth setup with normalized radius (r/r_0) and height (z/z_0). Although the 100 mm setup shows a larger ΔT range than the 2-inch one, the thermal stress cannot be evaluated solely from temperature range. Thermal stresses are affected by the spatial nonuniformity of the temperature field and the

resulting nonuniform thermal strain in the crystal. Therefore, maintaining a comparable temperature-field curvature during scale-up is essential for suppressing stress-induced dislocation multiplication. In our work, the hot-zone design was optimized to preserve the temperature-field curvature as much as possible despite the increase in crystal diameter. As a result, the values of temperature curvature for the 100 mm crystals were scarcely higher compared to the values for the 2-inch crystals: in the radial direction (2 inch: 4.9 K cm^{-2}, 100 mm: 7.2 K cm^{-2}) and in the axial direction (2 inch: 4.0 K cm^{-2}, 100 mm: 5.6 K cm^{-2}). These values suggest that, while increasing the thermal stresses due to diameter increase is inevitable, it is possible to have a maintainable thermal stress state after scale-up.

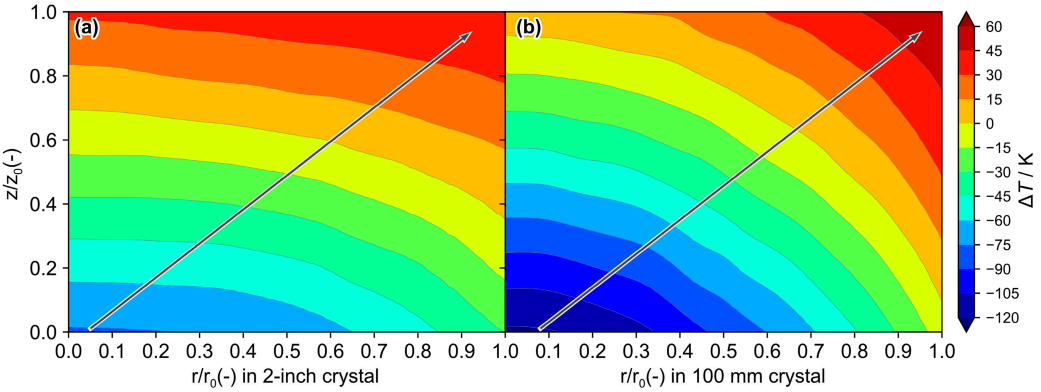

Figure 3. Numerical simulation results of the axisymmetric ΔT distribution inside AlN crystals in (**a**) 2-inch and (**b**) 100 mm crystal growth setup at the growth stage. Arrows indicate shift from low ΔT towards high ΔT.

To evaluate the thermoelastic stresses in the crystal at the growth stage, we applied a 3D-FEM tool, ABAQUS (version 2024), using the global temperature field, the 2D-FEM and Equation (5). The 2D-FEM cannot calculate stresses with circumferential directions. For this reason, we used a combination of the 2D-FEM and ABAQUS to simulate the thermal fields and stress–strain fields, respectively. Using stress components in Cartesian coordinates, the RSSs of $\langle 11\bar{2}0\rangle\{1\bar{1}00\}$ prismatic slip system and $\langle 11\bar{2}0\rangle\{0001\}$ basal system are obtained by following equations:

$$\tau_{RS}\langle 11\bar{2}0\rangle\{1\bar{1}00\} = \sigma_{xy}, \quad (6)$$

$$\tau_{RS}\langle 11\bar{2}0\rangle\{0001\} = \sigma_{xz}, \quad (7)$$

The RSS on prismatic slip system is calculated and depicted as shown in Figure 4. The estimated CRSS from the homology method (Equation (4)) and Peierls stress in the range of 1800–2400 °C (Equations (2) and (3)) are also shown. Both 2-inch and 100 mm setups demonstrate similar behavior: the RSS on prismatic slip system increases from the center toward the edge of the crystals. Such behavior for 2-inch AlN crystals was predicted by Karvani and Maniatty [43] who simulated the tensile stresses on the *m*-planes. This prediction allowed dislocation density estimation within the bulk of the crystal which followed the trend given by the stress, i.e., lowest dislocation density in the center of the crystal with gradual increase towards the crystal edges. Such dislocation density distribution for the 2-inch AlN crystals was recently confirmed by Jacobs et al. who used X-ray topography (XRT) in reflection geometry and found that the dislocation density increases from 10^2 cm^{-2} in the wafer center to about 10^5 cm^{-2} at the wafer edges [44]. Comparing the absolute values of the RSS on prismatic system, those in the 100 mm setup are greater than those in the 2-inch setup. The maximum shear stresses of prismatic systems in the 2-inch and 100 mm setups are 28 MPa and 55 MPa, respectively.

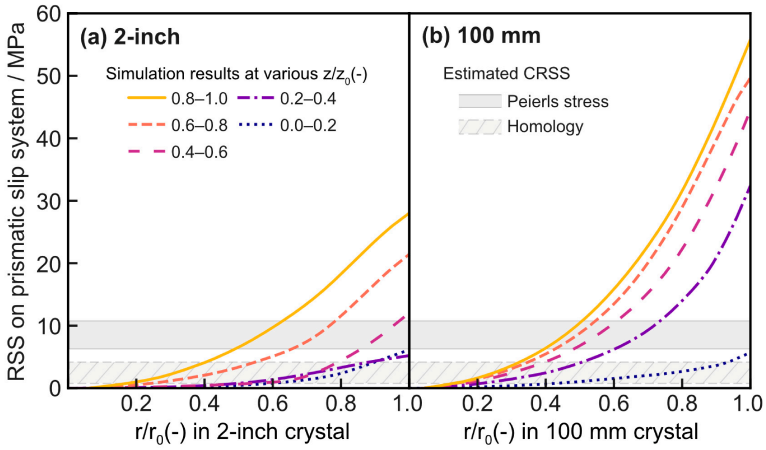

Figure 4. Simulation results of RSS in AlN crystals with prismatic system for (**a**) 2-inch and (**b**) 100 mm setup at the growth stage. The estimated CRSS were depicted as solid and dash gray lines for homology method and calculation results with Peierls stress.

The entire trends in curves of RSS (Figure 5) for the basal slip system showed that the stress increases linearly with distance from the center to the edge up to r/r_0 = 0.7–0.8 (Figure 5). After that, the RSS decreases in the outer edge region (0.8–1.0). Such M-shape curves for the dome side of the crystal were also observed in the simulation of the SiC-PVT system [45–47] which are, in general, typical for many other semiconductors grown in different environments [34]. The maximum RSS on basal slip system in the 2-inch and 100 mm setups are 37 MPa and 60 MPa, respectively. The ratio between the RSS maxima for both prismatic and basal plane slip systems closely follow the ratio between the temperature-field curvatures found utilizing Figure 3. Based on this data, as well as the data for the prismatic slip presented in Figure 4, it is clear how big the role of thermoelastic stress is. New dislocations will be generated if the resolved shear stress is larger than the critical resolved shear stress. Since the resolved shear stress is minimal and smaller than the CRSS in the middle/center of the substrate, we expect low or zero dislocation density in those regions. However, there are many other dislocation generation mechanisms such as faulty nucleation, presence of obstacles (e.g., impurities, inclusion, point defects, etc.), and various multiplication and transformation mechanisms. All of these can cause a certain dislocation density background which makes it difficult to fully separate and classify the dislocation generation mechanisms.

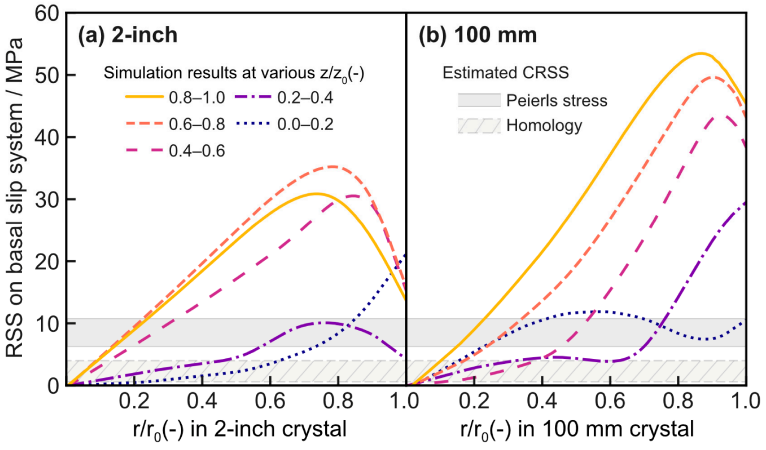

Figure 5. Simulation results of RSS in AlN crystals with basal system for (**a**) 2-inch and (**b**) 100 mm setups. The estimated CRSS were depicted as solid and dash gray lines for homology method and calculation results with Peierls stress.

3. AlN Substrate Characterization Results

In general, the structural characterization of the AlN substrates includes the X-ray diffraction (XRD) technique as being non-destructive, and able to quickly assess the material quality. Previously [3], we reported the full width of the half maximum (FWHM) of symmetric (002) and asymmetric (102) rocking curves to vary between 29 and 80 arcseconds. Recently, these values were confirmed by Njuguna et al. [48] demonstrating (002) narrow rocking curves with FWHM of about 27 arcseconds.

In addition to XRD, we used X-ray topography (XRT) to further evaluate the large AlN substrates (Figure 6). Synchrotron white beam XRT in transmission geometry was used to image all defects in the bulk of the substrate as well as to count the basal plane dislocations (BPD). Synchrotron monochromatic beam X-ray topography in grazing incidence geometry was used to view the threading defects that intersect the surface. This allows for counting both threading edge and threading screw dislocations.

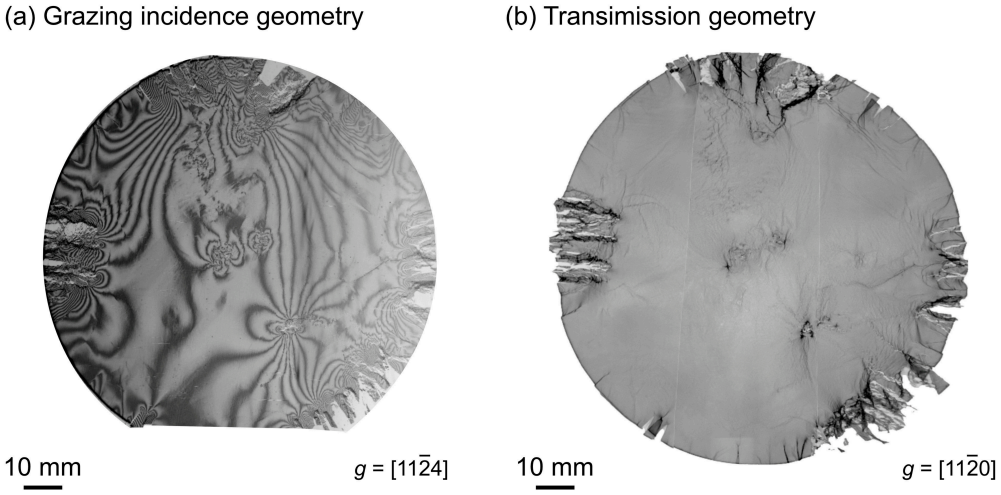

Figure 6. X-ray topographs: (**a**) Grazing incidence geometry with a diffraction vector $[11\bar{2}4]$ and (**b**) transmission geometry with a diffraction vector $[11\bar{2}0]$.

The grazing geometry topograph (Figure 6a) shows narrow contours near the edges and around high-stress regions and relatively wide contours for the rest of the area. The high-stress regions are interpreted as dislocation bunches. Such defects were also found in the 2-inch AlN wafers and were later eliminated. Similarly, further development can help improve the 100 mm AlN material quality. The monochromatic X-ray topograph shown in Figure 6b allows observation of high-stress regions corresponding to the same regions found in the grazing topograph. These high-stress regions represent low-angle grain boundaries (LAGBs). LAGBs are often observed when the crystal grows laterally with high radial thermal gradient. Further improvements in the crystal growth technique are needed to minimize and reduce these defects. The average threading dislocation density measured in nine spots is about 4.0×10^3 cm^{-2}. The average BPD density was counted in a similar way and is about 1.0×10^3 cm^{-2} with highly uniform distribution for most of the wafer area. Many regions including the wafer center demonstrate zero basal plane dislocations. It is worth noticing that, based on our previous experience, the dislocation density in the regions containing low-angle grain boundaries or dislocation bunches is usually at least one order of magnitude higher compared to the dislocation density of the matrix material. Therefore, we expect that the total dislocation densities in these 100 mm AlN substrates to be in the range 10^4–10^5 cm^{-2}. Regarding the dislocation distribution, it appears that we have a low threading dislocation and zero BPD density in the central

area of the substrate. These densities increase towards the wafer edges as predicted by the resolved shear stress calculations for the prismatic and basal slip systems (Figures 4 and 5).

Both dislocation density and distribution were confirmed using etch pit density (EPD) evaluation. The EPD evaluation was done using KOH–NaOH eutectic melt at about 500 °C. The N-polar face was protected, and the etch pits were revealed on the Al-face. We followed the procedure described in great detail earlier [21]. The average etch pit density (Figure 7a,b) varies in the range 10^4–10^5 cm^{-2}, and this variation is applicable for different wafers from the same crystal as well as for wafers cut from different crystals. Additionally, in some regions etching revealed both slip bands aligned along *m*-planes (Figure 7c), as well as polygonization (Figure 7d), reaffirming the existence of slip along the prismatic glide system.

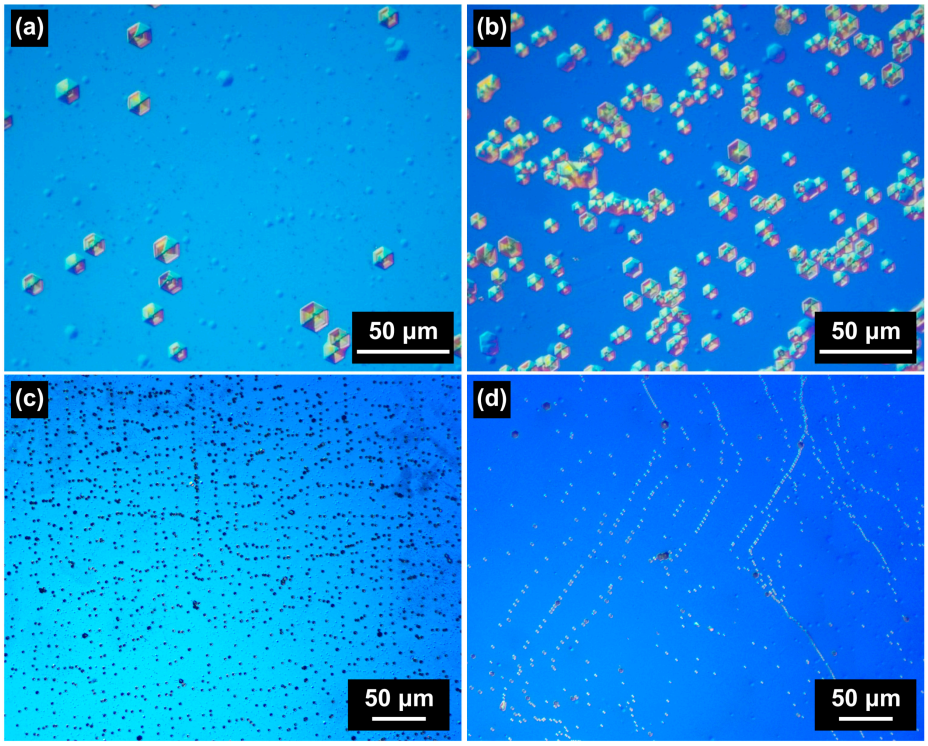

Figure 7. Etch pit dislocation micrographs showing (**a**) a region of 10^4 cm^{-2} EPD, (**b**) a region of 10^5 cm^{-2} EPD, (**c**) m-plane-aligned slip bands, (**d**) m-plane polygonization.

AlN substrates are being developed for their potential use in power electronics where the thermal conductivity plays a critical role; hence, we report the results here. Thermal conductivity measurements were performed by Laser Thermal (Charlottesville, VA, USA) using a combination of steady-state thermoreflectance (SSTR) and time-domain thermoreflectance (TDTR), with a thin layer of aluminum deposited on AlN wafers as a transducer. SSTR measured the total thermal resistance of the combined transducer and AlN wafer, whereas TDTR primarily measures the thermal resistance in the direction perpendicular to the sample surface. The combination of the two techniques allows for the separation of the Al transducer film contribution to thermal resistance, as well as the resolution of in-plane and through-plane thermal conductivity.

Fragments from a 100 mm substrate were measured at room temperature. The thermal conductivity was measured in two directions, perpendicular and parallel to the c-axis. The two types of measurements returned very similar values of 300 ± 15 W m^{-1} K^{-1}. Therefore, these thermal conductivity values are comparable to the values previously measured [3] using the Xenon flash technique that conformed to the ASTM standards E1461-13 [49].

The initial commercial development of AlN single-crystal substrates was aimed at fabrication of light-emitting diodes (LED) operating in the UVC band of the ultraviolet spectrum (UVC). The UVC-LED have proven their effectiveness in the areas of germicidal irradiation used in water, surface, and air disinfection [2]. Further industrialization would require mass production of the UVC-LED at affordable cost. One way to achieve these goals is to use AlN substrates with diameters larger than 2 inch. Hence, our 100 mm substrate development seeks AlN material that is highly transparent in the UVC region of the spectrum and particularly at 265 nm wavelength, which is usually the wavelength of choice used in germicidal devices. The UV transparency is obtained using a spectrophotometer with a beam size of about 1 mm (JASCO V-670, Jasco International, Tokyo, Japan). A motorized stage helps generate mapping data across the substrates. Figure 8 shows the UV absorption data for a typical 100 mm AlN substrate plotted against a similar AlN substrate that is 2 inch in diameter.

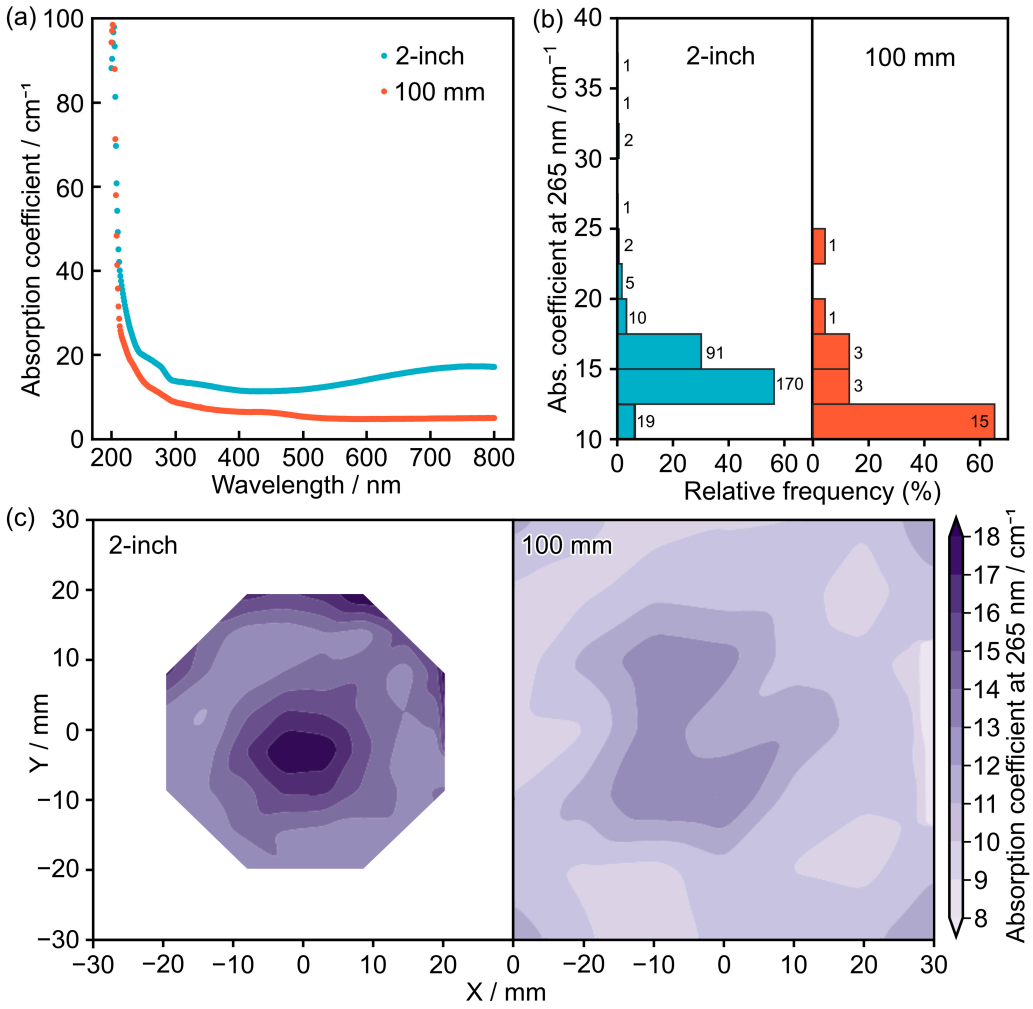

Figure 8. UV absorption properties of 100 mm AlN substrate plotted against the 2-inch substrate: (**a**) absorption spectra, (**b**) relative frequency distributions of absorption coefficient at 265 nm, and (**c**) average absorption coefficient maps at 265 nm wavelength.

As can be observed from Figure 8, the absorption coefficient for the 100 mm AlN substrate demonstrates similar or better values at 265 nm wavelength and for the whole spectrum in the range of 200–800 nm. The absorption coefficient is below 20 cm^{-1} for the entire area of the 100 mm wafer. Both the high UVC transparency and thermal conductivity values are attributed to the low impurity levels, specifically carbon and oxygen having concentrations in around 10^{17} cm^{-3}.

4. Summary

Aluminum nitride single crystals with diameter over 100 mm were grown using the PVT technique. The crystals were sliced into wafers and polished for the purpose of either electronic device substrates or native AlN seeds. The substrates demonstrate ample crystalline quality with narrow XRD double-crystal rocking curves with FWHM in the range of about 30–80 arcseconds. The threading and basal plane dislocation densities estimated using X-ray topography and confirmed by EPD technique does not exceed 10^4–10^5 cm^{-2}. The role of the thermoelastic stress in dislocation generation is demonstrated using 2D and 3D-FEM simulation tools. The resolved shear stress for both prismatic and basal plane slip systems increase towards the crystal edges and follows an M-shape curve known for other semiconductor materials. Since true engineering stress–strain curves for AlN are not yet available, the critical resolved shear stress was estimated using Peierls–Nabarro stress as well as homology models. Both models appear in good agreement with critical resolved shear stress being about 1–10 MPa for the relevant temperature range 1800–2400 °C. Nevertheless, we expect the experimental data on CRSS to be gathered as soon as possible to quantify the thermoelastic stress analysis and its role in dislocation generation during crystal growth. AlN substrates with diameter of 100 mm are currently available for further developments of power, RF and opto-electronic devices. In this report we confirmed the high thermal conductivity of ~300 ± 15 W m^{-1} K^{-1} at room temperature, making AlN material a natural substrate choice for ultrawide bandgap power and RF electronic devices. Furthermore, the 100 mm AlN substrates are highly transparent in the UVC range of the spectrum, resulting in absorption coefficients as low as 10 cm^{-1} at 265 nm wavelength.

Author Contributions: Conceptualization, R.T.B. and S.M.; methodology, S.M. and C.G.C.; software, S.M. and M.K.; validation, J.G. and K.H.; formal analysis, R.T.B. and S.M.; investigation, G.Q.N.; writing—original draft preparation, R.T.B.; writing—review and editing, R.T.B., S.M., K.H. and J.G. All authors have read and agreed to the published version of the manuscript.

Funding: This research received no external funding.

Data Availability Statement: The original contributions presented in the study are included in the article. Further inquiries can be directed at the corresponding author.

Conflicts of Interest: Robert T. Bondokov is an employee of Crystal IS, Inc., Shogen Matsumoto is an employee of Crystal IS, Inc. and Asahi Kasei Corporation, Connor G. Carr is an employee of Crystal IS, Inc., Kasey Hogan is an employee of Crystal IS, Inc., Griffin Q. Norbury is an employee of Crystal IS, Inc., Masato Kobayashi is an employee of Asahi Kasei Corporation, and James Grandusky is an employee of Crystal IS, Inc. All authors declare that the research was conducted in the absence of any commercial or financial relationships that could be construed as a potential conflict of interest.

References

1. Tsao, J.Y.; Chowdhury, S.; Hollis, M.A.; Jena, D.; Johnson, N.M.; Jones, K.A.; Kaplar, R.J.; Rajan, S.; Van De Walle, C.G.; Bellotti, E.; et al. Ultrawide-Bandgap Semiconductors: Research Opportunities and Challenges. *Adv. Electron. Mater.* **2018**, *4*, 1600501. [CrossRef]
2. Bondokov, R.T.; Branagan, S.P.; Ishigami, N.; Grandusky, J.; Nagatomi, T.; Tatsuta, K.; Miebach, T.; Chen, J. Two-Inch Aluminum Nitride (AIN) Single Crystal Growth for Commercial Applications. *ECS Trans.* **2021**, *104*, 37–48. [CrossRef]
3. Bondokov, R.T.; Hogan, K.; Norbury, G.Q.; Matsumoto, S.; Grandusky, J. Development of 100 mm AlN Single-Crystal Growth and Subsequent Substrate Preparation. *Phys. Status Solidi B* **2025**, *262*, 2500032. [CrossRef]
4. Kim, E.; Chen, Y.; Pieczulewski, N.; Encomendero, J.; Muller, D.A.; Jena, D.; Xing, H.G. XHEMTs on Ultrawide Bandgap Single-Crystal AlN Substrates. *Adv. Electron. Mater.* **2026**, *12*, e00393. [CrossRef]
5. Chen, Y.-H.; Shinohara, K.; Encomendero, J.; Pieczulewski, N.; Hogan, K.; Grandusky, J.; Muller, D.A.; Xing, H.G.; Jena, D. From Atomic-Scale Understanding to Wafer-Scale Growth: Delta-Doped AlN/GaN/AlN XHEMTs on Single-Crystal AlN by Molecular Beam Epitaxy. *APL Mater.* **2025**, *13*, 121103. [CrossRef]

6. Kim, M.; Papamichail, A.; Tran, D.Q.; Paskov, P.P.; Darakchieva, V. Thin-Channel AlGaN/GaN/AlN Double Heterostructure HEMTs on AlN Substrates via Hot-Wall MOCVD. *Appl. Phys. Lett.* **2025**, *127*, 032104. [CrossRef]
7. Lee, T.; Yoshikawa, A.; Hagihara, Y.; Sugiyama, S.; Arai, M.; Ando, Y.; Suda, J.; Amano, H. Low-Resistance and Current-Collapse-Free MOVPE-Grown Pseudomorphic AlN/GaN/AlN HEMTs on AlN Substrates. In Proceedings of the 2025 IEEE International Electron Devices Meeting (IEDM), San Francisco, CA, USA, 6–10 December 2025.
8. Quiñones, C.E.; Khachariya, D.; Reddy, P.; Mita, S.; Almeter, J.; Bagheri, P.; Rathkanthiwar, S.; Kirste, R.; Pavlidis, S.; Kohn, E.; et al. High-Current, High-Voltage AlN Schottky Barrier Diodes. *Appl. Phys. Express* **2024**, *17*, 101002. [CrossRef]
9. Mazumder, A.A.M.; Jamil, T.; Rahman, M.; Ali, M.; Simin, G.; Khan, A. High Field Performance of Si-Doped *n*-AlN Layers Grown Using Pulsed MOCVD. *Appl. Phys. Express* **2025**, *18*, 065501. [CrossRef]
10. Da, B.; Herath Mudiyanselage, D.; Wang, D.; He, Z.; Fu, H. High-Voltage kV-Class AlN Metal-Semiconductor Field-Effect Transistors on Single-Crystal AlN Substrates. *Appl. Phys. Express* **2024**, *17*, 104002. [CrossRef]
11. Jamil, T.; Mazumder, A.A.M.; Rahman, M.; Ali, M.; Simin, G.; Khan, A. $Al_xGa_{1-x}N$ ($0.7 < x < 1$) Schottky Diodes Using Distributed Polarization Doped Layer with a Current Density of 14 kA/cm^2. *Appl. Phys. Lett.* **2026**, *128*, 133501. [CrossRef]
12. Hartmann, C.; Kabukcuoglu, M.P.; Richter, C.; Klump, A.; Schulz, D.; Juda, U.; Bickermann, M.; Hänschke, D.; Schröder, T.; Straubinger, T. Efficient Diameter Enlargement of Bulk AlN Single Crystals with High Structural Quality. *Appl. Phys. Express* **2023**, *16*, 075502. [CrossRef]
13. Fu, D.; Lei, D.; Li, Z.; Zhang, G.; Huang, J.; Sun, X.; Wang, Q.; Li, D.; Wang, J.; Wu, L. Toward Φ56 Mm Al-Polar AlN Single Crystals Grown by the Homoepitaxial PVT Method. *Cryst. Growth Des.* **2022**, *22*, 3462–3470. [CrossRef]
14. Wang, Q.; Lei, D.; He, G.; Gong, J.; Huang, J.; Wu, J. Characterization of 60 mm AlN Single Crystal Wafers Grown by the Physical Vapor Transport Method. *Phys. Status Solidi A* **2019**, *216*, 1900118. [CrossRef]
15. Wang, Q.; Lei, D.; Huang, J.; Sun, X.; Li, D.; Zhou, Z.; Wu, L. Homoepitaxial Growth of 3-Inch Single Crystalline AlN Boules by the Physical Vapor Transport Process. *Front. Mater.* **2023**, *9*, 1128468. [CrossRef]
16. HEXATECH, INC. News and Events. Available online: https://www.hexatechinc.com/news-events.html#feb102026 (accessed on 8 May 2026).
17. Li, W.; Liu, Q.; Tan, J.; He, G.; Wang, Y.; Sun, Z.; Li, B.; Wu, H. Synergistic Crucible Design and Thermal-Flow Management for Enhanced 4-Inch AlN Single Crystal PVT Growth: A Combined Numerical and Experimental Investigation. *CrystEngComm* **2025**, *27*, 3219–3228. [CrossRef]
18. Zhu, Y.; Cao, W.; Wang, G.; Wu, Y.; Lv, L.; Du, J.; Wang, S.; Xu, X.; Zhang, L. Effect of Growth Domain Height on 4-Inch AlN Single Crystal Growth by PVT Method. *Cryst. Growth Des.* **2026**. [CrossRef]
19. Liu, S.; Yuan, Y.; Sheng, S.; Wang, T.; Zhang, J.; Huang, L.; Zhang, X.; Kang, J.; Luo, W.; Li, Y.; et al. Four-Inch High Quality Crack-Free AlN Layer Grown on a High-Temperature Annealed AlN Template by MOCVD. *J. Semicond.* **2021**, *42*, 122804. [CrossRef]
20. Lu, S.; Ben, J.; Jiang, K.; Zhang, S.; Zhang, R.; Hao, J.; Liu, Z.; Sun, W.; Nie, Z.; Sun, X.; et al. 6-Inch AlN Epitaxial Films with Low Dislocation Densities via MOCVD. *J. Semicond.* **2025**, *46*, 022501. [CrossRef]
21. Bondokov, R.T.; Mark, J.; Hogan, K.; Norbury, G.; Grandusky, J. Growth of Bulk AlN Crystals. In *Comprehensive Semiconductor Science and Technology*; Elsevier: Amsterdam, The Netherlands, 2025; pp. 132–158, ISBN 978-0-323-95819-6.
22. Schmid, E.; Boas, W. *Plasticity of Crystals with Special Reference to Metals*; F. A. Hughes & Co. Limited: London, UK, 1950.
23. Bondokov, R.T.; Morgan, K.E.; Shetty, R.; Liu, W.; Slack, G.A.; Goorsky, M.; Schowalter, L.J. Defect Content Evaluation in Single-Crystal AlN Wafers. *Mater. Res. Soc. Symp. Proc.* **2006**, *892*, 0892-FF30-03.1. [CrossRef]
24. Zhao, Y.; Fu, D.; Wang, Q.; Huang, J.; Lei, D.; Ren, Z.; Wu, L. Glide Mobility of A-Type Edge Dislocations in Aluminum Nitride by Molecular Dynamics Simulation. *ACS Omega* **2022**, *7*, 2015–2022. [CrossRef] [PubMed]
25. Audrier, V.; Demenet, J.L.; Rabier, J. AlN Plastic Deformation between Room Temperature and 800 °C I. Dislocation Substructure Observations. *Philos. Mag. A* **1998**, *77*, 825–842. [CrossRef]
26. Raghothamachar, B.; Dudley, M.; Rojo, J.C.; Morgan, K.; Schowalter, L.J. X-Ray Characterization of Bulk AlN Single Crystals Grown by the Sublimation Technique. *J. Cryst. Growth* **2003**, *250*, 244–250. [CrossRef]
27. Hu, S.; Fang, H.; Liu, Y.; Peng, H.; Ailihumaer, T.; Cheng, Q.; Chen, Z.; Dalmau, R.; Britt, J.; Schlesser, R.; et al. Prismatic Slip in AlN Crystals Grown By PVT. *ECS Trans.* **2021**, *104*, 57–64. [CrossRef]
28. Hu, S.; Fang, H.; Liu, Y.; Peng, H.; Cheng, Q.; Chen, Z.; Dalmau, R.; Britt, J.; Schlesser, R.; Raghothamachar, B.; et al. Characterization of Prismatic Slip in PVT-Grown AlN Crystals. *J. Cryst. Growth* **2022**, *584*, 126548. [CrossRef]
29. Herms, M.; Kabukcuoglu, M.P.; Hartmann, C.; Stöhr, M.; Wagner, M.; Hamann, E.; Hänschke, D.; Richter, C.; Straubinger, T. Comparative Study of Residual Stress and Defects in Single-Crystalline (0001) AlN Wafers by Scanning Infrared Depolarization and White-Beam X-ray Topography. *Phys. Status Solidi A* **2025**, *222*, 2400787. [CrossRef]
30. Samant, A.V.; Pirouz, P. Activation Parameters for Dislocation Glide in A-SiC. *Int. J. Refract. Met. Hard Mater.* **1998**, *16*, 277–289. [CrossRef]
31. Wang, J.N. A Microphysical Model of Harper-Dorn Creep. *Acta Mater.* **1996**, *44*, 855–862. [CrossRef]

32. MacChesney, J.B.; Bridenbaugh, P.M.; O'Connor, P.B. Thermal Stability of Indium Nitride at Elevated Temperatures and Nitrogen Pressures. *Mater. Res. Bull.* **1970**, *5*, 783–791. [CrossRef]
33. Kirchner, H.O.K.; Suzuki, T. Plastic Homology of Tetrabonded Crystals. *Acta Mater.* **1998**, *46*, 305–311. [CrossRef]
34. Jordan, A.S.; Caruso, R.; Neida, A.R.V. A Thermoelastic Analysis of Dislocation Generation in Pulled GaAs Crystals. *Bell Syst. Tech. J.* **1980**, *59*, 593–637. [CrossRef]
35. Wang, Q.; Huang, J.; Wang, Z.; He, G.; Lei, D.; Gong, J.; Wu, L. Anisotropic Three-Dimensional Thermal Stress Modeling and Simulation of Homoepitaxial AlN Single Crystal Growth by the Physical Vapor Transport Method. *Cryst. Growth Des.* **2018**, *18*, 2998–3007. [CrossRef]
36. Zhao, Y.; Wang, Q.; Zhang, G.; Huang, J.; Fu, D.; Wu, J. Comparison of the Thermal Stress Behavior of AlN Single Crystal Growth on AlN and SiC Seeds via the Physical Vapor Transport Method Through Three-Dimensional Numerical Modeling and Simulation. *Cryst. Growth Des.* **2021**, *21*, 2653–2662. [CrossRef]
37. Qin, Z.Y.; Li, W.L.; Sun, Z.H.; Ji, J.H.; Wu, H.L.; Jin, L. Analysis of Residual Thermal Stress for AlN Crystal Growth by PVT. *Vacuum* **2023**, *214*, 112237. [CrossRef]
38. Wu, B.; Ma, R.; Zhang, H.; Dudley, M.; Schlesser, R.; Sitar, Z. Growth Kinetics and Thermal Stress in AlN Bulk Crystal Growth. *J. Cryst. Growth* **2003**, *253*, 326–339. [CrossRef]
39. Wu, B.; Ma, R.; Zhang, H.; Prasad, V. Modeling and Simulation of AlN Bulk Sublimation Growth Systems. *J. Cryst. Growth* **2004**, *266*, 303–312. [CrossRef]
40. Cao, W.; Wang, S.; Yu, R.; Wang, G.; Hu, X.; Zhu, Y.; Wu, Y.; Zhao, X.; Xu, X.; Zhang, L. Effect of Air Layer Thickness on AlN Crystal Growth by the PVT Method. *Cryst. Growth Des.* **2024**, *24*, 4613–4621. [CrossRef]
41. Cao, W.; Wang, S.; Yu, R.; Wang, G.; Zhu, Y.; Wu, Y.; Lv, L.; Du, J.; Xu, X.; Zhang, L. Suitable AlN Source Shape for Optimizing Gas Mass Transfer During AlN Crystal Growth. *Cryst. Growth Des.* **2024**, *24*, 9059–9066. [CrossRef]
42. Cao, W.; Wang, S.; Cui, P.; Wang, G.; Zhu, Y.; Wu, Y.; Lv, L.; Wang, L.; Xu, X.; Zhang, L. Extended Temperature Field Facilitates 90 Mm AlN Crystal Growth and HEMT Device Validation. *Cryst. Growth Des.* **2025**, *25*, 1136–1147. [CrossRef]
43. Karvani, P.; Maniatty, A.M. Modeling Micromechanical Response to Thermal History in Bulk Grown Aluminum Nitride. *Phys. Status Solidi C* **2015**, *12*, 345–348. [CrossRef]
44. Jacobs, A.G.; Gann, K.R.; Rocco, E.G.; Pennachio, D.J.; Hogan, K.; Grandusky, J.R.; Mahadik, N.A.; Culbertson, J.C.; Freitas, J.A.; Woodward, J.M.; et al. Wafer Scale Characterization of Bulk AlN Substrates and Homoepitaxial Growth. *Appl. Phys. Lett.* **2026**, *128*, 202102. [CrossRef]
45. Ma, R.-H.; Zhang, H.; Dudley, M.; Prasad, V. Thermal System Design and Dislocation Reduction for Growth of Wide Band Gap Crystals: Application to SiC Growth. *J. Cryst. Growth* **2003**, *258*, 318–330. [CrossRef]
46. Steiner, J.; Roder, M.; Nguyen, B.D.; Sandfeld, S.; Danilewsky, A.; Wellmann, P.J. Analysis of the Basal Plane Dislocation Density and Thermomechanical Stress during 100 Mm PVT Growth of 4H-SiC. *Materials* **2019**, *12*, 2207. [CrossRef] [PubMed]
47. Miyazaki, K.; Nakano, S.; Nishizawa, S.; Kakimoto, K. Effect of Crucible Thermal Conductivity on Dislocation Distribution in Crystals in a Silicon Carbide Physical Vapor Transport Furnace. *J. Cryst. Growth* **2023**, *603*, 126981. [CrossRef]
48. Njuguna, T.; Alwan, H.; Hogan, K.; Grandusky, J.; Li, J.; Lin, J.Y.; Jiang, H.X. Structural and Optical Properties of 100 mm AlN Bulk Single Crystals. *Appl. Phys. Lett.* **2025**, *127*, 182102. [CrossRef]
49. *ASTM E1461-13*; Standard Test Method for Thermal Diffusivity by the Flash Method. ASTM International: West Conshohocken, PA, USA, 2022. [CrossRef]

Disclaimer/Publisher's Note: The statements, opinions and data contained in all publications are solely those of the individual author(s) and contributor(s) and not of MDPI and/or the editor(s). MDPI and/or the editor(s) disclaim responsibility for any injury to people or property resulting from any ideas, methods, instructions or products referred to in the content.